J. Fluid Mech. (2024), *vol*. 979, A18, doi:10.1017/jfm.2023.1048

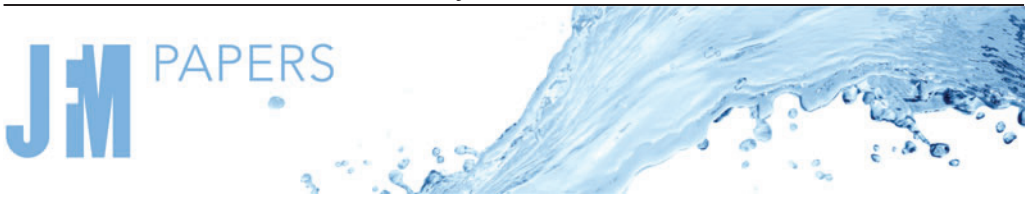

Single cavitation bubble dynamics in a stagnation flow

Dominik Mnich[1],†, Fabian Reuter[1], Fabian Denner[2] and Claus-Dieter Ohl[1]

[1]Faculty of Natural Sciences, Institute for Physics, Otto-von-Guericke-University Magdeburg, Universitätsplatz 2, 39106 Magdeburg, Germany

[2]Department of Mechanical Engineering, Polytechnique Montréal, Montréal, H3T 1J4, QC, Canada

(Received 14 July 2023; revised 6 December 2023; accepted 6 December 2023)

Jetting of collapsing bubbles is a key aspect in cavitation-driven fluid–solid interactions as it shapes the bubble dynamics and additionally due to its direct interaction with the wall. We study experimentally and numerically the near-wall collapse and jetting of a single bubble seeded into the stagnation flow of a wall jet, i.e. a jet that impinges perpendicular onto a solid wall. High-speed imaging shows rich and rather distinct bubble dynamics for different wall jet flow velocities and bubble-to-wall stand-off distances. The simulations use a volume-of-fluid method that allows us to numerically determine the microscopic and transient pressures and shear stresses on the wall. It is shown that a wall jet at moderate flow velocities of a few metres per second already shapes the bubble ellipsoidally inducing a planar and convergent jet flow. The distinct bubble dynamics allow us to tailor the wall interaction. In particular, the shear stresses can be increased by orders of magnitude without increasing impact pressures the same way. Interestingly, at small seeding stand-offs, the bubble during the final collapse stage can lift off the wall and migrate against the flow direction of the wall jet such that the violent collapse occurs away from the wall.

Key words: bubble dynamics, cavitation

1. Introduction

In the vicinity of a solid boundary, cavitation bubbles in stagnant liquids collapse non-spherically. They result in jetting and shockwave emissions and expose the boundary to significant wall shear stresses and pressures. The dynamics of the simple case of a bubble collapsing near a rigid planar surface has been the subject of many studies in the

† Email address for correspondence: dominik.mnich@ovgu.de

last decades; see, for example, (Plesset & Chapman 1971; Lauterborn & Bolle 1975; Zhang, Duncan & Chahine 1993; Supponen *et al.* 2016). Jets pierce the bubble and are typically directed toward the rigid boundary. They can reach velocities of 50–100 m s^{-1} (Benjamin & Ellis 1966; Blake & Gibson 1987; Lauterborn & Kurz 2010) for millimetre-sized bubbles at atmospheric pressure, known as regular jetting. The most important parameter that determines the bubble dynamics in a stagnant liquid and in the absence of gravity is the non-dimensional stand-off distance $\gamma = d/R_{max}$, where d is the initial distance of bubble nucleation from the wall and R_{max} is the radius of the bubble at its maximum expansion. For the smallest bubble-to-wall stand-off distances, even velocities of more than one order of magnitude larger are possible, known as needle jetting (Lechner *et al.* 2019; Reuter & Ohl 2021; Bußmann *et al.* 2023). Most violent collapses, i.e. erosive cavitation, occur when a bubble during its collapse focuses the self-emitted shockwaves onto itself to produce a shockwave self-intensified collapse. This was observed for bubbles of very small stand-off distances, i.e. $\gamma \lesssim 0.2$ by Reuter, Deiter & Ohl (2022*a*).

A particularly interesting case is when the bubble takes the shape of a slender spherical cap during maximum expansion, which leads to a liquid jet that is directed away from the boundary. This kind of jet has been predicted for mildly ellipsoidal capped bubbles by Lauer *et al.* (2012) and Aganin, Kosolapova & Malakhov (2019), and was later shown to occur for axisymmetric cap-shaped bubbles in simulations and experiments by Saini *et al.* (2022). Here, a high-pressure region below the bubble forms that accelerates a liquid jet flow away from the surface. Other configurations involving elastic boundaries (Gibson & Blake 1982; Brujan *et al.* 2001) or a narrow gap (Chahine 1982; Gonzalez-Avila *et al.* 2011*b*; Zeng, Gonzalez-Avila & Ohl 2020) result in hourglass-shaped bubbles that pinch-off and give rise to two fast and rather thin jets in opposite directions.

The broad range of bubble dynamics allows for a wide field of useful applications, such as surface cleaning (Ohl *et al.* 2006*a*; Kim *et al.* 2009; Gonzalez-Avila *et al.* 2011*a*; Reuter & Mettin 2016; Reuter *et al.* 2017; Ando *et al.* 2021, 2023) or drug delivery via sonoporation (Prentice *et al.* 2005; Ohl *et al.* 2006*b*; Gac *et al.* 2007). For these applications, large wall shear stresses are beneficial, especially if they can be generated without exposing the wall to an excessively large pressure that may cause damage to even the hardest materials (Tomita & Shima 1986; Philipp & Lauterborn 1998; Reuter *et al.* 2022*a*). Wall shear stresses from a single bubble collapse have been measured (Dijkink & Ohl 2008; Reuter & Mettin 2018) and simulated (Koukouvinis *et al.* 2018; Zeng, An & Ohl 2022) to reach peak values of 100 kPa. Experimental data yield peak values that are one order of magnitude smaller, which is still compatible, as sampling periods were one order of magnitude larger than the shear spike durations.

While these observations are valid for bubbles in an initially stagnant liquid, the presence of a flow can change the bubble dynamics and, thus, the wall shear stress and pressure generated at the wall drastically. One interesting case is hydrodynamic cavitation in a stagnation flow, as it was shown by Knapp (1955) that the strongest erosion for a model in a water tunnel can be found in the area around stagnation points. So far, research on the effect of a flow on the dynamics of a single bubble was conducted through simulations by Blake, Taib & Doherty (1986), Robinson & Blake (1994) and Blake, Leppinen & Wang (2015).

They utilised a boundary element method to study the influence of an ideal stagnation point flow on the gross bubble dynamics and, in particular, on the bubble's jetting behaviour. They found hourglass-shaped bubbles that pinch-off, resulting in much faster and thinner jets. Experimental research on the dynamics of bubbles in flows near a

stagnation point is rather scarce. Starrett (1982) reported in his thesis of a striking contrast between the bubble dynamics in a quiescent liquid and in a stagnation flow. He observed that during expansion the bubble deforms into an ellipsoid with the major axis aligned parallel to the wall, then the bubble forms a waist at its equator that divides the bubble into two parts just prior to collapse. Starret studied the dynamics of rather large bubbles created with an electric discharge in stagnation flows with free-stream velocities between about 6–18 m s^{-1} and concentrated on larger distances rather than on small stand-offs, which are more relevant for the bubble–wall interaction.

In the present work we study the dynamics of a single cavitation bubble in a wall jet in particular at rather low flow velocities and small stand-off distances, i.e. where viscosity plays an important role. This regime is relevant for many applications. In experiments, we record the bubble dynamics with a suitable high-speed camera to resolve the details of the collapse, whereas the simulations, which include the effects of compressibility and viscosity, allow for determining the wall shear stresses and pressure acting on the wall as a consequence of the bubble collapse. The results reveal that a bubble collapse with beneficial high wall shear stresses can be realised while avoiding potentially damaging behaviour.

2. Methods

2.1. *Experimental methods*

A single, laser-induced cavitation bubble is produced in a wall jet flow at a well-controlled distance to a wall. The submerged wall jet (Glauert 1956) is issued from a conical nozzle and provides a laminar water stream perpendicular to the wall that spreads radially outwards, see figure 1, i.e. providing a stagnation point flow. The cavitation bubble is laser seeded on the central axis of the wall jet at a variable distance from the wall.

For convenience, the water is collected in a transparent water tank and recirculated. About 1.2 litres of water are used and pumped with a rotary vane pump (aquastream XT, Aqua Computer GmbH, Germany) through the nozzle. The nozzle is fully submerged in the water of the tank to ease observation of the bubble dynamics within the wall jet. The back part of the nozzle assembly is open to air; see figure 1(*a*). Inside the nozzle, the water passes through a honeycomb filter (stacked cylinders with 2 mm diameter and 30 mm length) to straighten the flow. The volumetric flow rate Q is measured with a turbine flow meter (FCH-midi-POM, B.I.O-TECH e.K.) located between the pump and the nozzle inlet. The average wall jet velocity is given by $v_{jet} = Q/A_{nozzle}$, where $A_{nozzle} = \pi r_{nozzle}^2$ is the cross-sectional area of the circular nozzle with an inner radius of $r_{nozzle} = 1.5$ mm. In our set-up, v_{jet} can be controlled between 0 and 5 m s^{-1} using the software provided with the pump.

To generate single cavitation bubbles, one pulse from a frequency-doubled Nd:YAG laser (wavelength of 532 nm) is first collimated and guided through a hollow tube from the back end of the nozzle assembly. Then the laser is focused, and a bubble explosively grows as a result of the optic breakdown. Focusing is achieved using a planoconvex lens of focal length $f = 10$ mm (in air) with a diameter of 6 mm (Thorlabs, LA1116). The lens is bonded into the wall-facing end of a tube. The planar side of the lens is in contact with water, while the curved side is in contact with air on the hollow tube side. The distance of the lens to the nozzle exit is 11 mm. When the laser is fired, a cavitation bubble is created at a distance of 4.4 mm from the nozzle exit. Due to the strong deformation of the bubbles, in experiments and simulations, the volume-equivalent bubble radius was measured. The geometry of the three-dimensionally printed nozzle (PLA plastic) went through a number

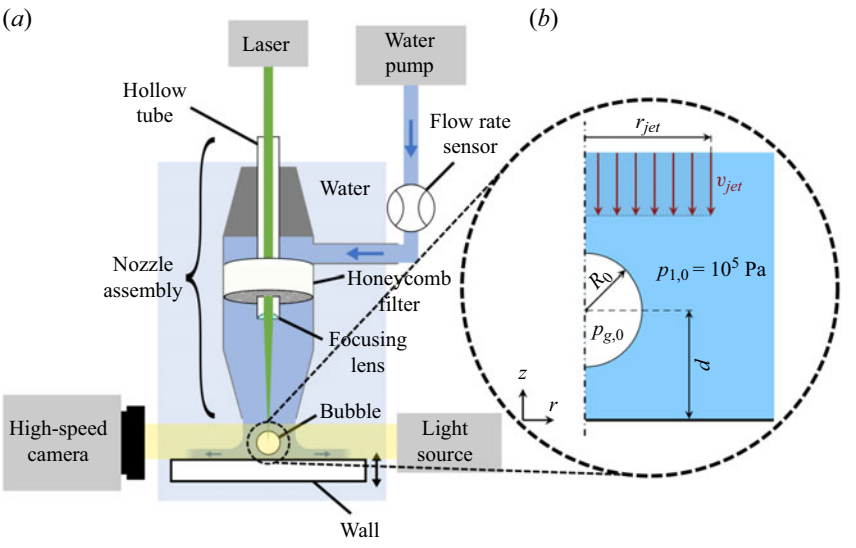

Figure 1. (*a*) Sketch of the experimental set-up. The cavitation bubble is generated by focusing the laser pulse through a lens into the wall jet. The wall jet flow is submerged to ease optical access using a high-speed camera. The liquid flow is driven with a pump and controlled with a flow rate sensor feedback loop. A honeycomb filter straightens the flow, resulting in a laminar wall jet flow. The distance of the bubble to the wall is adjusted by moving the glass plate, while the nozzle assembly remains fixed. (*b*) Schematic illustration of the bubble in the wall jet and the axisymmetric simulation set-up (not to scale).

of iterations to achieve a smooth water flow along the lens such that no air gets entrapped at the lens output aperture. A linear convergent nozzle together with a honeycomb flow rectifier accomplishes this requirement. In addition, there is no significant recirculation or disturbance of the stagnation flow since the bubble size is much smaller than the outer nozzle diameter (7 mm) and the solid sample. To confirm the laminar flow profile, we have used micrometre-sized particles as flow tracers together with high-speed imaging; see Appendix A.

The wall is provided by a square-shaped coverslip with side length 24 mm and a thickness of 0.16 mm. It is mounted onto a plastic frame such that a central 'window' of 14 mm × 14 mm remains for observation through the wall. The size of the glass sample is much larger than the nozzle diameter such that edge effects of the sample do not influence the flow in the gap between nozzle and sample surface. The distance between the laser plasma, i.e. bubble generation, and the glass wall is adjusted with a translation stage. The bubble dynamics is recorded with a high-speed camera (Shimadzu HPV-X2) imaging through the water-filled tank and the discharged wall jet flow from the nozzle. As a light source, we used an intense, pulsed light emitting diode (LED-P40, SMETec).

2.2. *Simulation methods*

Numerical simulations complement the experimental recordings. The primary aim of these simulations is to investigate the differences in wall shear stress and pressure generated by a collapsing bubble in a wall jet flow, as compared with in an initially stagnant body of liquid. Experimentally, these quantities are inaccessible due to the required temporal and spatial resolutions.

The considered compressible two-phase flow is governed by the continuity equation

$$\frac{\partial \rho}{\partial t} + \boldsymbol{\nabla}\boldsymbol{\cdot}(\rho \boldsymbol{u}) = 0 \tag{2.1}$$

and the momentum equation

$$\frac{\partial \rho \boldsymbol{u}}{\partial t} + \boldsymbol{\nabla}\boldsymbol{\cdot}(\rho \boldsymbol{u} \otimes \boldsymbol{u}) = -\boldsymbol{\nabla} p + \boldsymbol{\nabla}\boldsymbol{\cdot}\left[\mu(\boldsymbol{\nabla}\boldsymbol{u} + \boldsymbol{\nabla}\boldsymbol{u}^{\mathrm{T}}) - \frac{2}{3}\mu(\boldsymbol{\nabla}\boldsymbol{\cdot}\boldsymbol{u})\boldsymbol{I}\right], \tag{2.2}$$

where t represents time, ρ is the mass density of the fluid, μ is the dynamic viscosity of the fluid, $\boldsymbol{u}$ is the velocity of the flow, p is the pressure and $\boldsymbol{I}$ is the identity tensor. An algebraic volume-of-fluid method (Denner, Xiao & van Wachem 2018) is adopted to model the gas–liquid interface and distinguish the gas and the liquid. The governing conservation laws are closed using the Noble–Abel stiffened gas (NASG) equation of state (Le Métayer & Saurel 2016) in polytropic form, with the density and speed of sound defined as

$$\rho = \frac{K(p + \Pi)^{1/\kappa}}{1 + bK(p + \Pi)^{1/\kappa}}, \tag{2.3}$$

$$c = \sqrt{\kappa \frac{p + \Pi}{\rho(1 - b\rho)}}, \tag{2.4}$$

respectively, where κ is the polytropic exponent, Π is a pressure constant and $K = \rho_0/[(p_0 + \Pi)^{1/\kappa}(1 - b\rho_0)]$ defines a constant reference state based on a reference pressure p_0 and density ρ_0.

We are choosing the polytropic form of the NASG equation of state because we are not focusing on the details of the decay of the emitted pressure pulses that may (or may not) form shock fronts as they propagate away from the bubble, and since the Péclet number associated with the liquid jet that pierces the bubble during collapse is high, $Re > 10^3$, we do not consider heat transfer to be an important factor for our simulations. Using such a polytropic fluid model has been demonstrated to be suitable even for the prediction of complex bubble behaviour, such as wall-bounded cavitation (Koch *et al.* 2016; Zeng *et al.* 2018). Following previous work we are neglecting surface tension and justify this simplification by (i) the relatively large bubble size with a volume-equivalent diameter >1 mm at maximum expansion, and (ii) the high Weber number, $We > 10^3$, of the liquid jet that pierces the bubble during collapse.

The liquid is assumed to be water, with $\kappa_l = 1.186$, $\Pi_l = 7.028 \times 10^8$ Pa, $b_l = 6.61 \times 10^{-4}\ \mathrm{m^3\,kg^{-1}}$, $\rho_{0,l} = 957.74\ \mathrm{kg\,m^{-3}}$, $c_{0,l} = 1540.2\ \mathrm{m\,s^{-1}}$ and $p_{0,l} = 10^5$ Pa, as previously proposed by Le Métayer & Saurel (2016), and $\mu_l = 10^{-3}$ Pa s. The bubble content is taken to be non-condensable air, modelled as an ideal gas ($\Pi_g = 0$, $b_g = 0$), with $\kappa_g = 1.4$, $\rho_{0,g} = 1.2\ \mathrm{kg\,m^{-3}}$, $p_{0,g} = 10^5$ Pa and $\mu_g = 1.82 \times 10^{-5}$ Pa s. The governing equations are discretised using a second-order finite-volume method and solved using a fully coupled implicit pressure-based algorithm (Denner *et al.* 2018; Denner, Evrard & van Wachem 2020*a*).

The computational set-up is illustrated schematically in figure 1(*b*). The axisymmetric simulations are carried out in a $0.25\,\mathrm{m} \times 0.25\,\mathrm{m}$ computational domain, which is sufficiently large such that the boundary conditions do not influence the bubble dynamics or the flow field in the vicinity of the bubble in the considered time frame. The bubble is initialised at a distance d from the wall with initial gas pressure $p_{g,0} = 54.5$ MPa and

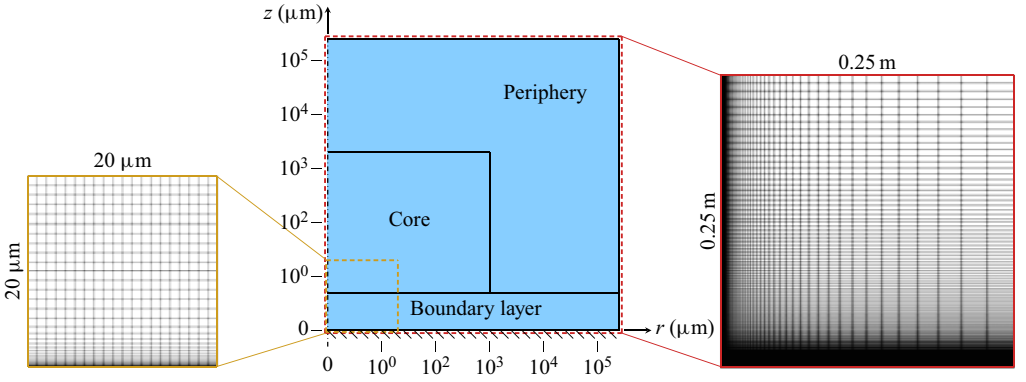

Figure 2. Schematic illustration of the computational domain with the three primary mesh regions (sketched on a logarithmic scale), with a close up of the computational mesh near the wall on the left and the complete computational mesh on the right.

initial radius $R_0 = 84\,\mu\text{m}$, tuned to achieve a desired maximum radius R_{max}. Based on the experimental set-up, the wall jet flow is represented by a uniform flow with velocity magnitude v_{jet} and radius $r_{jet} = 1500\,\mu\text{m}$.

The mesh resolution required to resolve the considered cases adequately is primarily governed by the diameter of the liquid jet penetrating the bubble, $\gtrsim 10\,\mu\text{m}$, and the velocity gradient normal to the wall, $O(10^7)$–$O(10^9)\,\text{s}^{-1}$, associated with the generated wall shear stresses. The computational mesh is static (i.e. does not adapt) and separated into three primary regions, as illustrated in figure 2: the boundary layer close to the rigid wall, the core region with the bubble and stagnation flow, and the periphery that mainly exists to avoid pressure waves reaching the domain boundaries. Note that, due to the large range of length scales, the computational domain is sketched on a logarithmic scale in figure 2. In line with previous studies on wall-bounded bubble collapse (Zeng *et al.* 2018; Lechner *et al.* 2020; Gonzalez-Avila, Denner & Ohl 2021; Mifsud *et al.* 2021), the core region of the domain ($r \leq 1000$ and $z \leq 2000\,\mu\text{m}$) is resolved with a mesh spacing of $\Delta x_0 = 1\,\mu\text{m}$ and the mesh near the wall ($z < 5\,\mu\text{m}$) is gradually refined, such that the centres of the layer of cells closest to the wall are located at a distance of only 12.5 nm from the wall. In the periphery region of the domain ($r > 1000$ and $z > 2000\,\mu\text{m}$), the mesh is gradually coarsened. Similar to our previous work (Gonzalez-Avila *et al.* 2021), the adaptively chosen time step is $\Delta t = Co\,\Delta x/|\boldsymbol{u}|$, where $Co = 0.7$ is the applied convective Courant number.

The employed numerical methods and case set-up were validated successfully against experiments of laser-induced bubble expansion and collapse near walls in our previous work, regarding the bubble evolution and shape as well as the acoustic emissions of the bubble collapse (Gonzalez-Avila *et al.* 2021), and regarding the minimum thickness of the thin liquid film remaining between bubble and wall (Reuter & Kaiser 2019; Denner, Evrard & van Wachem 2020*b*). Furthermore, the numerical methods have been compared favourably to experimental measurements and numerical predictions of shock-driven bubble collapse (Denner *et al.* 2018) and to the Gilmore model for a Rayleigh collapse (Denner & Schenke 2023). The specific resolution requirements of the simulated bubble dynamics are discussed alongside the simulation results in § 3 and representative results obtained with different mesh resolutions are reviewed in § 4.

2.3. *Scaling with bubble size*

Here, we consider bubbles with maximum radii ranging between $R_{max} = 480$ and $716\,\mu$m. To ease the discussion, we show that for a bubble in the considered wall jet, the same scaling as for a Rayleigh bubble holds.

The potential energy of a laser-induced cavitation bubble with negligible vapour pressure ($p_{vap} \ll p_\infty$) is customarily approximated as (Liang *et al.* 2022)

$$E_{pot} = \tfrac{4}{3}\pi R_{max}^3 p_\infty \propto R_{max}^3 p_\infty. \tag{2.5}$$

We estimate the kinetic energy imparted on the bubble by the wall jet as the product of the dynamic pressure of the wall jet and a suitably defined reference volume,

$$E_{jet} = \frac{\rho_{0,l}}{2} v_{jet}^2 V_{ref}. \tag{2.6}$$

We further assume that the wall jet acts on the upper hemisphere of the bubble, with a projected area of $A = \pi R_{max}^2$. Since the distance over which the bubble is advected by the wall jet during the bubble lifetime is negligible ($R_{max} \gg v_{jet} T_C$), R_{max} is the reference length scale of the problem. Thus, the reference volume is then defined as

$$V_{ref} = A R_{max}, \tag{2.7}$$

such that $E_{jet} \propto \rho_{0,l} v_{jet}^2 R_{max}^3$. For simplicity, we do not take surface tension and viscosity into account, since a collapsing cavitation bubble is an inertia-driven process; see, for example, Reuter, Zeng & Ohl (2022*b*). Taking the ratio of E_{jet} and E_{pot} yields

$$\frac{E_{jet}}{E_{pot}} \propto \frac{\rho_{0,l} v_{jet}^2}{p_\infty}. \tag{2.8}$$

Consequently, neglecting surface tension and viscous dissipation, the influence of the wall jet can be assumed to be independent of the bubble size. Therefore, the presented results are, in first approximation, independent of the bubble size.

This allows us to normalize the times on the bubble lifetime T_L, i.e. the time between bubble nucleation and first collapse (minimum volume) as $T_L \propto R_{max}$, to facilitate the comparison of similarly sized bubbles.

3. Results

The results are organised by reporting the effect of the flow velocity of the wall jet, v_{jet}, on the bubble dynamics for three different stand-off distances γ. (1) The first stand-off is far from the wall at a large distance of $\gamma \approx 1.7$. Here, the bubble shows a pinch-off, as shown in previous studies for cavitation bubbles in a stagnation flow (Starrett 1982; Blake *et al.* 1986; Robinson & Blake 1994; Blake *et al.* 2015). (2) The second stand-off is at an intermediate distance of $\gamma \approx 0.7$, which shows a needle-like high-speed jet, as observed in stagnant liquid for smaller stand-off distances, $\gamma \lessapprox 0.2$ (Lechner *et al.* 2019; Reuter & Ohl 2021; Bußmann *et al.* 2023). (3) Last, a cavitation bubble representing the small stand-off distance dynamics ($\gamma \approx 0.4$) is presented. Here, the bubble pinches off directly above the wall, resulting in a lift-off of the bubble before it collapses. This is probably the most interesting case regarding the bubble–wall interaction, since a potentially harmful collapse in direct contact with the wall can be avoided. For each stand-off distance, high-speed imaging and numerical results of the bubble dynamics are shown and analysed, and the spatio-temporal wall shear stress and wall pressure distributions are discussed. Note that the given values may be considered as lower bounds of these quantities, which is discussed in more detail in § 4.

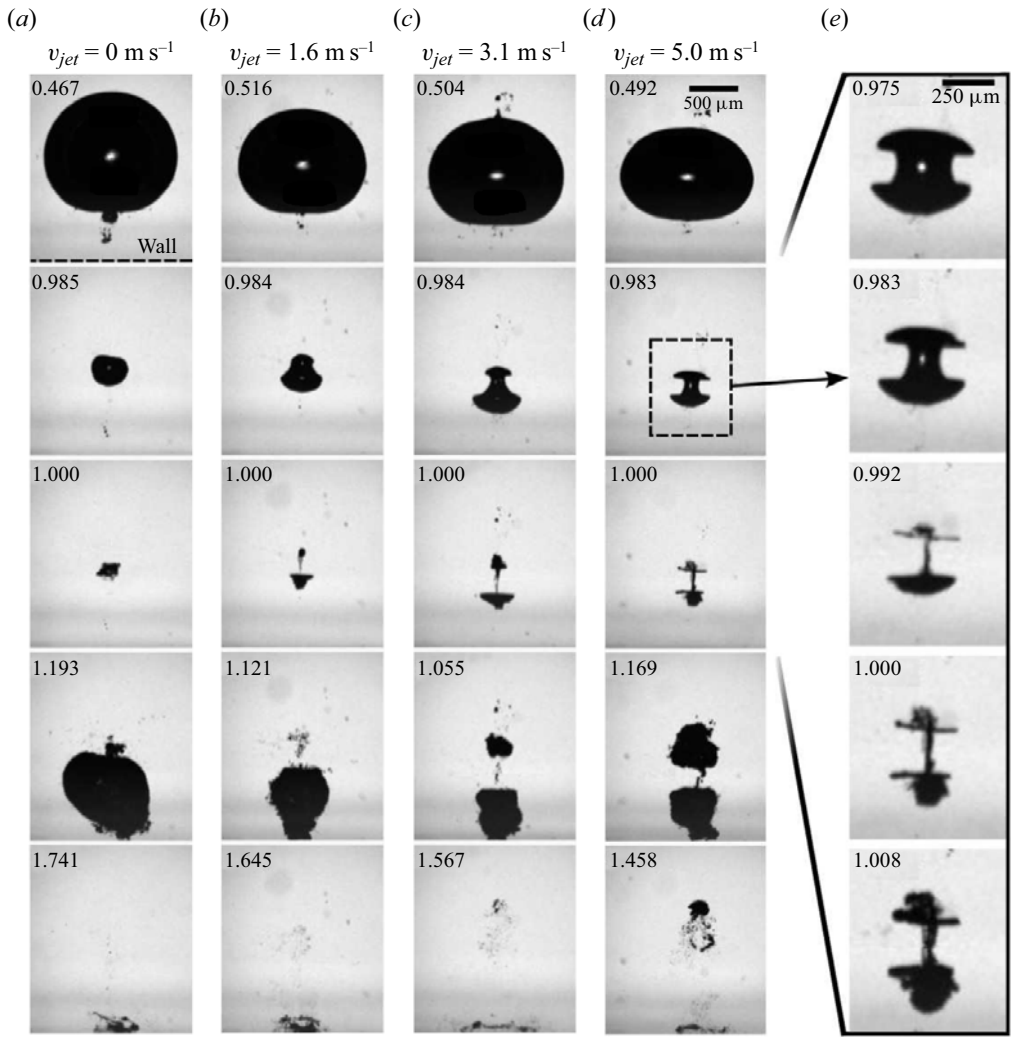

Figure 3. High-speed imaging of bubble dynamics for four different wall jet velocities v_{jet} at large stand-off distances (γ = 1.73, 1.78, 1.56, 1.88, from left to right). For sufficiently large wall jet velocities, the bubble pinches off and two axial jets develop in opposite directions. Times indicated in each tile are normalized to the bubble lifetime. The respective lifetimes are T_L = 135, 124, 127, 118 µs. The bottom of each frame coincides with the wall, as sketched in the first tile. The rightmost column shows the bubble splitting and collapse for the last case in more detail. A video of the dynamics at $v_{jet} = 5\,\mathrm{m\,s^{-1}}$ can be found in the supplementary material as movie 1 available at https://doi.org/10.1017/jfm.2023.1048.

3.1. *Large stand-off distance*

Figure 3 depicts the typical bubble dynamics for large stand-off distances. In the selected series, γ is between 1.56 and 1.88 and the glass wall is located at the bottom of each frame. Each column shows five snapshots from one experiment, showing the bubble at maximum expansion, the bubble just before and just after the collapse (from top to bottom), as well as the instance when the bubble makes contact with the wall and the second collapse. Each column in figure 3 shows one experiment with a specific wall jet velocity v_{jet}. Four wall jet velocities are shown, increasing from left to right.

The first column without jet flow ($v_{jet} = 0\,\mathrm{m\,s^{-1}}$) depicts the well-known jetting behaviour of a bubble nucleated at a large stand-off distance (here $\gamma = 1.73$) from the wall, as previously reported, for instance, by Philipp & Lauterborn (1998). At maximum expansion, $t = 0.467\,T_L$, the bubble is rather spherical but with some small bubbles at the wall-near pole. Here, the usage of a small lens with a rather small opening angle to focus the laser results in some aberration and multiple breakdowns. During collapse, the presence of the wall impedes the radial inflow from below, and a pressure gradient forms, with a higher pressure at the top. As a result, the bubble's centroid moves towards the wall (Benjamin & Ellis 1966) and the bubble develops a jet that passes through the bubble interior toward the wall. The specific illumination applied in the experiments does not reveal this jet flow, but it is visible by the small axial indentation of the upper pole just before the collapse. At time $t = 1.193\,T_L$ the main bubble reaches the wall while re-expanding. Later, it collapses a second time, now in proximity to the wall at $t = 1.741\,T_L$.

The simulated dynamics of the corresponding bubble is shown in figure 4(*a–c*). Here the jet formation is clear and jet velocities reach up to $100\,\mathrm{m\,s^{-1}}$, which is in close agreement with previous studies (Zeng *et al.* 2018; Gonzalez-Avila *et al.* 2021). Stresses on the wall are given in figure 5(*a*). The peak wall pressure is reached at $t = 1.003\,T_L$ and associated with the bubble collapse, rather than the jet impact pressure at $t = 1.101\,T_L$, in agreement with our previous work (Gonzalez-Avila *et al.* 2021). However, as the jet impacts the wall, it generates significant wall shear stresses, with a maximum of 94 kPa.

Let us now look at how the wall jet flow modifies the bubble dynamics, considering the case of the largest wall jet flow velocity $v_{jet} = 5\,\mathrm{m\,s^{-1}}$ first. In comparison to the stagnant case, the bubble takes an ellipsoidal shape with the major axis aligned parallel to the wall, i.e. it is flattened at the bottom, see the first row. A video of the corresponding bubble is available as movie 1 of the supplementary material. As the bubble collapses, instead of an indentation in the axial direction from the regular axial jet flow, a planar convergent jet indents the bubble from the sides and results in the horizontal kink in the second row. As this flow converges towards the axis of symmetry, two oppositely directed jets are ejected axially, see third row. More insights into this process are gained from the flow and pressure fields of figure 4(*d–f*) and the snapshot series at smaller time intervals showing the jet formation and piercing process in figure 4(*g–i*) as well as the rightmost column of figure 3. The convergent planar flow results in an axial needle-like jet with a radius of the order of 6 µm, indicated by an arrow in figure 4(*h*). The jet directed toward the wall reaches a maximum velocity of $\approx 300\,\mathrm{m\,s^{-1}}$, a threefold increase compared with the liquid jet generated in the corresponding case with no wall jet flow ($v_{jet} = 0\,\mathrm{m\,s^{-1}}$). Upon impact on the wall, the jet generates a maximum wall shear stress of 306 kPa, see figure 5(*b*), which is roughly three times higher than in the stationary case. Due to the formation of a stagnation point around the region where the axis of symmetry intersects the wall, the shear stresses are smaller there Reuter & Mettin (2018). Also, some negative shear rates are seen from splashing and recirculations of the complex flow after the jet impacts on the wall. The maximum pressures at the wall reach about $p_{max} = 9.3\,\mathrm{MPa}$ (a fourfold increase compared with $v_{jet} = 0\,\mathrm{m\,s^{-1}}$) and coincide with the jet impact. They are not generated from the shockwaves emitted during the collapse. The impact velocity of the jet can be approximated as $u = 135\,\mathrm{m\,s^{-1}}$ as the maximum pressure on the wall corresponds to the stagnation pressure of the jet, $p_{max} = 0.5\rho_{0,l}u^2$ (Gonzalez-Avila *et al.* 2021).

The pressure distribution in figure 4(*e*) reveals a larger pressure at the wall distal side around the bubble, which explains why, after pinch-off, the upper bubble collapses before

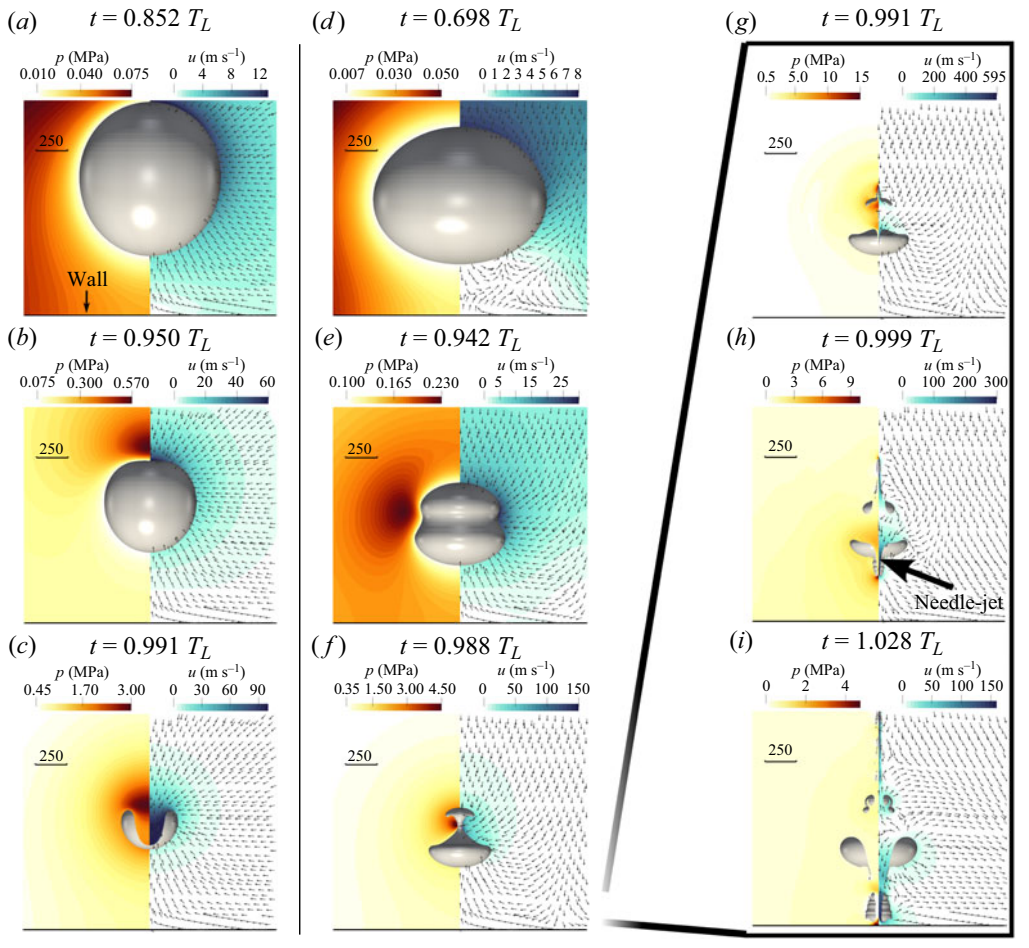

Figure 4. Bubble shape, pressure (left half) and velocity field (right half) at different time instances during the collapse of the bubble initially located at $d = 1200\,\mu\text{m}$ ($\gamma = 1.53$ and 1.75, respectively). The arrows in the right half of each figure indicate the direction of the flow. (*a–c*) In quiescent water ($v_{jet} = 0\,\text{m}\,\text{s}^{-1}$). The lifetime of this bubble is $T_L = 164.4\,\mu\text{s}$. (*d–i*) Subject to a wall jet with $v_{jet} = 5\,\text{m}\,\text{s}^{-1}$. The lifetime of this bubble is $T_L = 143.4\,\mu\text{s}$. The scale bar corresponds to $250\,\mu\text{m}$.

the lower bubble. For increasing wall jet velocity, the bubble becomes more ellipsoidal; see figure 3 first row. Furthermore, while at $v_{jet} = 5\,\text{m}\,\text{s}^{-1}$ the pinch-off occurs about the equatorial, which results in the bubble splitting into two about equally sized volumes, for lower wall jet velocities the pinch-off occurs closer to the upper bubble pole, which, in turn, results in an uneven splitting of the bubble. A smaller bubble is produced above and a larger bubble below the pinch-off region, as observed by comparing the second and fourth row in figure 3.

3.2. *Intermediate stand-off distance*

Figure 6 shows the evolution of the bubble dynamics for increasing wall jet flow velocities at intermediate stand-off distances of $\gamma \approx 0.75$. For each velocity the bubble is shown in four phases: (1) the moment of maximum expansion, (2) in the collapse phase when being increasingly deformed by the inflow, (3) the shape before, and (4) after the bubble collapse.

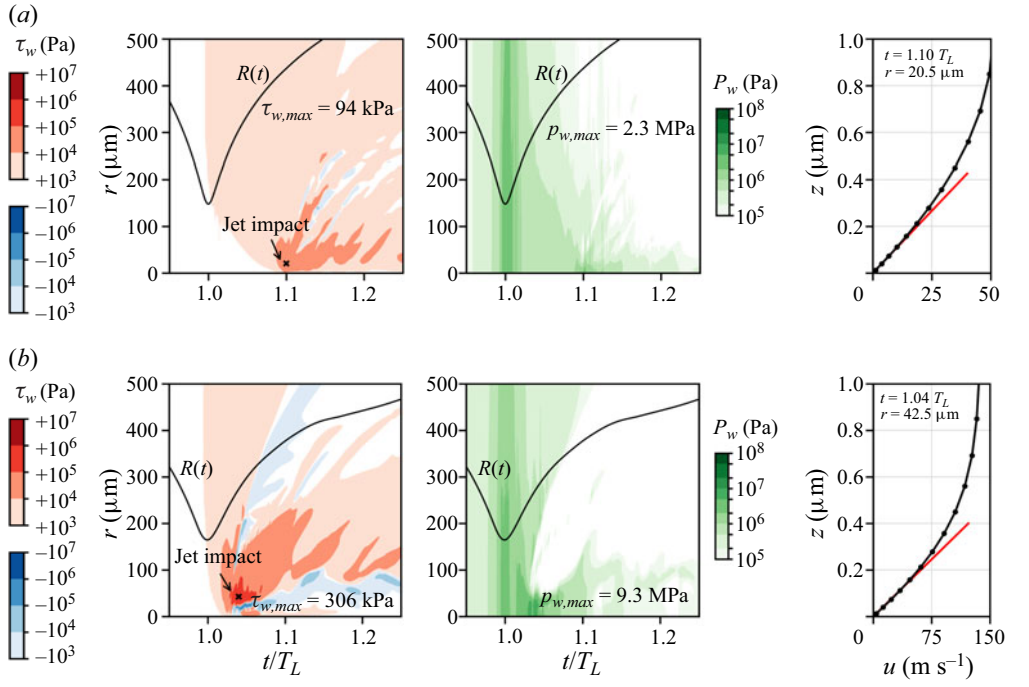

Figure 5. Space–time plots of the wall shear stress τ_w and the wall pressure p_w, and profile of the radial velocity u of the liquid at the location of the highest wall shear rate, of the bubble initially located at $d = 1200\,\mu$m. In the space–time plots, the black line shows the volume-equivalent bubble radius $R(t)$ and, with respect to τ_w, red (blue) areas indicate a radially outward (inward) going flow. The location of maximum wall shear stress is indicated with a bold cross in the space–time plots. In the plots of the velocity profiles, the red line represents the velocity gradient associated with $\tau_{w,max}$, and the black dots show the locations of the cell centres of the applied computational mesh. Results are shown for (*a*) $v_{jet} = 0\,\mathrm{m\,s^{-1}}$, $\gamma = 1.53$; (*b*) $v_{jet} = 5\,\mathrm{m\,s^{-1}}$, $\gamma = 1.75$.

Again, in the first column, a collapsing bubble in quiescent liquid is shown. At $t = 0.484\,T_L$, the bubble has reached approximately its maximum expansion. At $t = 0.916\,T_L$ the bubble is pierced by a rather wide jet, which is easily visible in the simulation result shown in figure 7(*b*). The velocity of this jet is $\approx$65 m s^{-1} and results in a toroidal collapse of the bubble in figure 6 at $t = 1.000\,T_L$. Upon impact at $t \approx 0.938\,T_L$ on the wall, the jet generates a wall shear stress of up to 62 kPa; see figure 8(*a*). The torus collapse close to the wall generates even larger shear stresses of up to 157 kPa at $r \approx 450\,\mu$m, further away from the location of the jet impact. Again, recirculations result in negative shear stresses. The shockwaves emitted at the collapse result in the vertically extended green region at $t = 1.000\,T_L$ in figure 8(*a*).

When adding a wall jet flow of $v_{jet} = 5\,\mathrm{m\,s^{-1}}$ (fourth column), similarly to the large γ case, the bubble assumes an ellipsoidal shape. The maximum extension in the axial direction is already reached at $t = 0.398\,T_L$ and the bubble is visibly pushed downward by the wall jet. As a result, the wall-near bottom of the bubble still extends along the wall, while the more distal parts already collapse (see movie 2 of the supplementary material). Again, a planar inflow shapes a kink into the bubble, which can be observed clearly in the simulations in figure 7(*d–f*). This bubble shape is very similar to a bubble in the stagnant liquid case without a wall jet flow but at a much smaller stand-off when forming a needle-like high-speed jet (Lechner *et al.* 2019; Reuter & Ohl 2021; Bußmann *et al.* 2023).

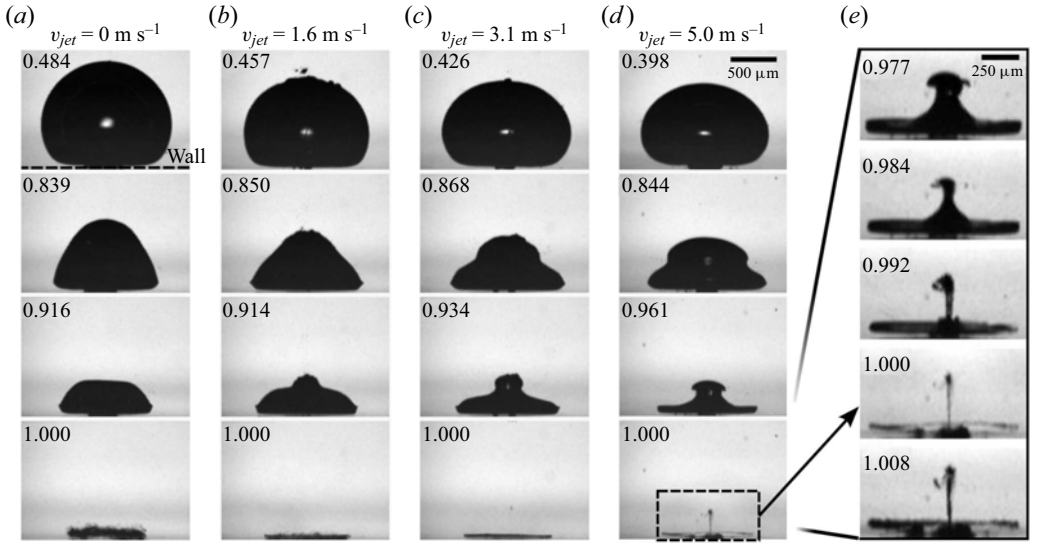

Figure 6. Bubble dynamics with increasing wall jet velocity at intermediate stand-offs ($\gamma = 0.74, 0.72, 0.78, 0.78$, from left to right). The wall extends along the bottom of the frames. For the fastest wall jet flow, a high-speed needle-like jet occurs. Times indicated in each tile are normalized to the bubble lifetime. The respective lifetimes are $T_L = 155, 140, 136, 128\,\mu$s (from left to right). The collapse for the case $v_{jet} = max$ is studied in further detail in the rightmost column. The corresponding video of the bubble at $v_{jet} = 5\,\mathrm{m\,s^{-1}}$ can be found in the supplementary material as movie 2.

Figure 7(*d–i*) confirms the formation of a thin needle-like jet, with peak velocities of 300–400 m s^{-1}. This needle jet yields a maximum wall shear stress of 2764 kPa as shown in figure 8(*b*) at $t \approx 0.97\,T_L$, which is 44 times higher compared with the conventional jetting case ($v_{jet} = 0\,\mathrm{m\,s^{-1}}$). Despite this very large wall shear stress, the associated velocity gradients are resolved adequately by the employed computational mesh, as evident by the velocity profile that coincides with the maximum wall shear stress on the right-hand side of figure 8(*b*). The maximum wall pressure of 49 MPa (a sixfold increase compared with the stationary case) is generated by the impact of this needle jet, see figure 8(*b*), from which the impact velocity of the needle jet on the wall can be estimated as $\approx$310 m s^{-1}. In contrast to the large γ case, now only an insignificant flow in the upward direction is generated.

From the evolution of the bubble shape with decreasing wall jet flow velocities in figure 6, it can be seen how the bubble becomes less ellipsoidal and the kink less pronounced. At $v_{jet} = 3.1$ and $v_{jet} = 5.0\,\mathrm{m\,s^{-1}}$ in the last row, a string-like gas phase is visible along the axis of symmetry but not for $v_{jet} = 1.6$ and $v_{jet} = 1.6\,\mathrm{m\,s^{-1}}$. Note that this string-like gas phase is an indicator that the planar jet has converged onto the axis of symmetry, as, for instance, visible along the axis of symmetry in figure 4(*i*). As the simulations suggest, this is a result of the pinch-off process, i.e. only in the two higher wall jet velocity cases does the planar jet converge on the axis of symmetry, while for the cases $v_{jet} \leq 1.6\,\mathrm{m\,s^{-1}}$ the regular jet passes the axis already before the planar jet can reach the axis of symmetry.

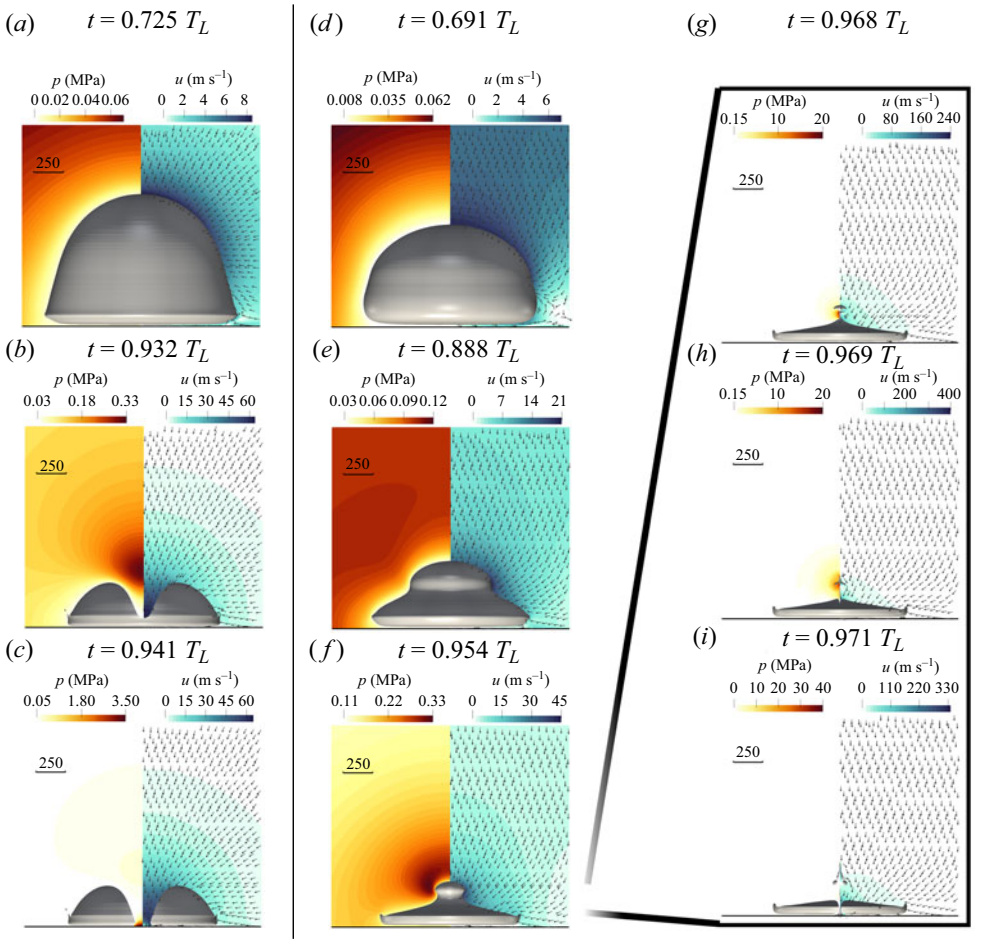

Figure 7. Bubble shape, pressure and velocity field at different time instances during the collapse of the bubble initially located at $d = 490\,\mu\text{m}$ ($\gamma = 0.63$ and 0.73, respectively). (*a–c*) In quiescent water ($v_{jet} = 0\,\text{m}\,\text{s}^{-1}$). The lifetime of this bubble is $T_L = 179.3\,\mu\text{s}$. (*d–i*) Subject to a wall jet with $v_{jet} = 5\,\text{m}\,\text{s}^{-1}$. The lifetime of this bubble is $T_L = 152.0\,\mu\text{s}$. The scale bar corresponds to $250\,\mu\text{m}$.

3.3. *Small stand-off distance*

The bubble dynamics for the smallest stand-offs presented here ($\gamma \approx 0.45$) are depicted in figure 9 for increasing wall jet velocities. The first row shows the maximum expansion, the second row the shape during shrinkage, the third and fourth rows depict the bubble just before and after the collapse, respectively, and the last row shows the bubble at the second collapse.

The quiescent case ($v_{jet} = 0\,\text{m}\,\text{s}^{-1}$) is similar to the quiescent intermediate γ case shown in figure 6. The simulation results are shown in figure 10(*a–c*). They reveal a jet velocity of $\approx 45\,\text{m}\,\text{s}^{-1}$ and a maximum wall shear stress of 54 kPa in the space–time plots in figure 11(*a*) at $t = 0.964\,T_L$, due to the jet impact before the bubble reaches its minimum volume. The maximum pressure peak of 11 MPa, however, is caused by the collapse of the bubble.

When introducing a wall jet flow with $v_{jet} = 5\,\text{m}\,\text{s}^{-1}$, in the fourth column of figure 9, the bubble during its expansion already moves significantly towards the wall and then

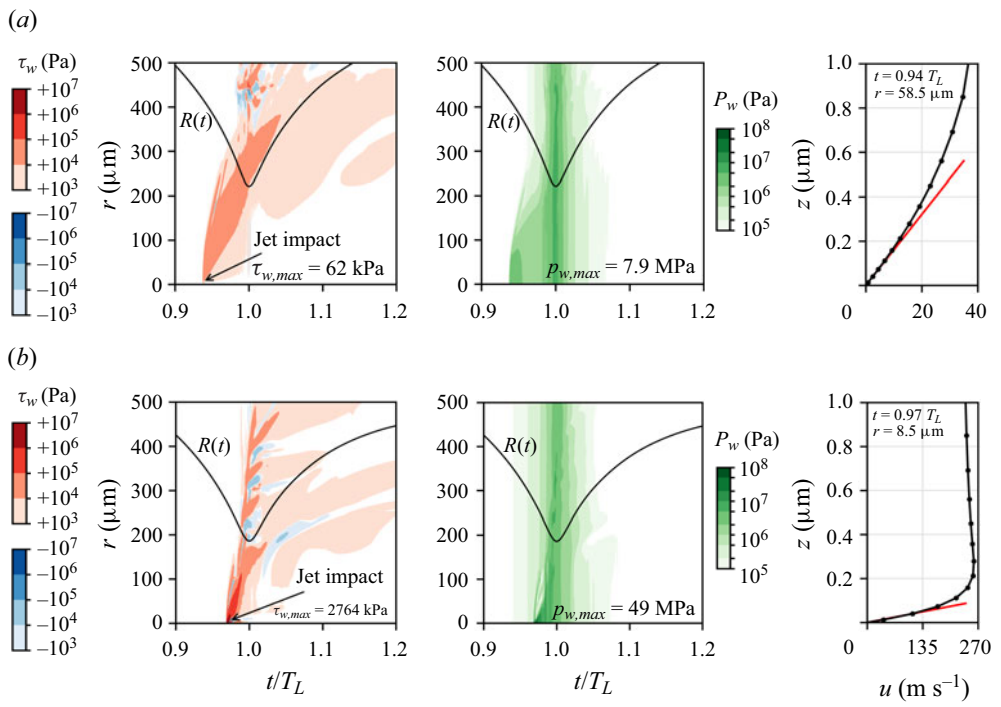

Figure 8. Space–time plots of the wall shear stress τ_w and the wall pressure p_w, and profile of the radial velocity u of the liquid at the location of the highest wall shear rate, of the bubble initially located at $d = 490\,\mu$m. In the space–time plots, the black line shows the volume-equivalent bubble radius $R(t)$ and, with respect to τ_w, red (blue) areas indicate a radially outward (inward) going flow. In the plots of the velocity profiles, the red line represents the velocity gradient associated with $\tau_{w,max}$, and the black dots show the locations of the cell centres of the applied computational mesh. Results are shown for (*a*) $v_{jet} = 0\,\mathrm{m\,s^{-1}}$, $\gamma = 0.63$; (*b*) $v_{jet} = 5\,\mathrm{m\,s^{-1}}$, $\gamma = 0.73$.

shows a quite different dynamics. A video of the corresponding bubble is available as movie 3 of the supplementary material. The bubble extends to a rather flat shape along the wall and a kink is formed during the collapse stage; see $t = 0.835\,T_L$ and figure 10(*e*). This kink again is related to the planar and converging jet flow that now develops directly at the wall. This planar jet now converges in very close distance to the wall and proceeds here even below the bubble, such that it gives the bubble a mushroom-like shape; see $t = 0.992\,T_L$ in figure 9 and the magnification in figure 10(*h*). Upon convergence of the planar jet, the bubble is lifted off the wall and an axial jet is formed, similar as before in the case of a larger stand-off, but this time in the reverse direction, i.e. away from the wall with velocities of $\approx$160 m s^{-1}; see figure 10(*i*). As a result, the final collapse occurs about 120 μm away from the wall; see $t = 1.000\,T_L$. Subsequently, the gas phase, now in the several bubbles arranged along a ring, translates further upward such that the second collapse occurs at a distance of 500 μm from the wall ($t = 1.409\,T_L$).

However, even if it is not possible to see directly in the presented graphs, the space–time plot in figure 11(*b*) indicates that also a downwards-directed jet hits the wall shortly after the bubble reaches its minimum volume, visible through the wall shear stress peak at $t = 1.01\,T_L$. Upon impact, the jet generates a wall shear stress of 1893 kPa, which is 35 times larger compared with the stationary case. At the same time, the maximum wall pressure reaches 86 MPa, which is about 8 times larger compared with cavitation bubbles

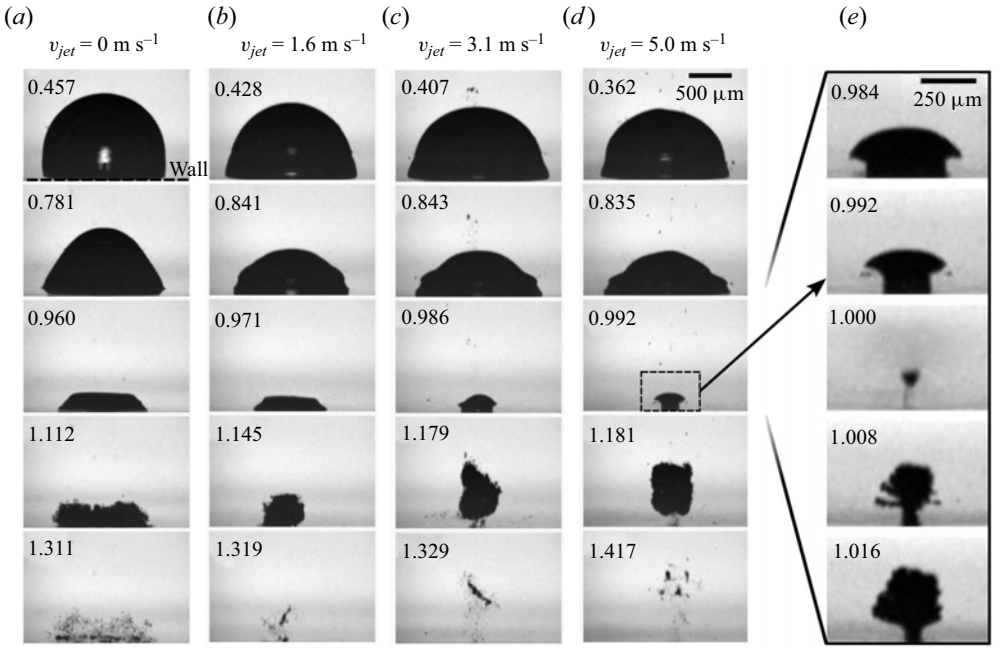

Figure 9. Bubble dynamics at small stand-off ($\gamma = 0.49, 0.46, 0.44, 0.46$, from left to right). For the fastest wall jet, an upwards-directed jet flow evolves. The normalized time is indicated in each frame, the respective lifetimes are $T_L = 151, 138, 140, 127\,\mu$s. The rightmost column shows the collapse for v_{max} in detail. The wall is located at the bottom of each frame. A video of the bubble at $v_{jet} = 5\,\mathrm{m\,s^{-1}}$ is provided in the supplementary material as movie 3.

in a quiescent liquid and which corresponds to the stagnation pressure of a jet with a velocity of $\approx$410 m s^{-1}.

Comparing the bubble shapes of the two middle columns just prior and after the collapse in figure 9, suggests that in the case of $v_{jet} = 1.6\,\mathrm{m\,s^{-1}}$ the regular jet that forms axially pierces the bubble already before the planar boundary-parallel inflow can converge; see $t = 0.992\,T_L$. After impact on the wall, the regular jet collides with and inhibits further planar inflow towards the axis of symmetry. In contrast, for $v_{jet} = 3.1\,\mathrm{m\,s^{-1}}$, the wall-parallel flow is sufficiently fast to meet on the axis of symmetry before the regular jet pierces the bubble, such that the wall-parallel flow can still lift the bubble off upon convergence. However, the collapse seems to occur closer to the wall than in the case with $v_{jet} = 5.0\,\mathrm{m\,s^{-1}}$.

3.4. *Parameter overview*

While in the last section, the effect of the wall jet flow on the bubble shape dynamics is studied, in figure 12 we compare the stand-off dependence of the bubble shape for the maximum wall jet velocity of $v_{jet} = 5\,\mathrm{m\,s^{-1}}$. For large stand-offs ($\gamma = 1.88$), kink and pinch-off occur rather symmetric, i.e. close to the bubble equator. As the bubble is generated closer to the wall, i.e. for decreasing γ, the bubble extends further along the wall. There, the bubble dynamics is slowed down and the wall distal part above the pinch-off region collapses faster, resulting in a small cap being shaped; see, for example, $\gamma = 0.89$. Only at the smallest stand-off ($\gamma = 0.46$) shown does the planar jet evolve sufficiently fast and sufficiently close to the wall to result in a bubble lift-off.

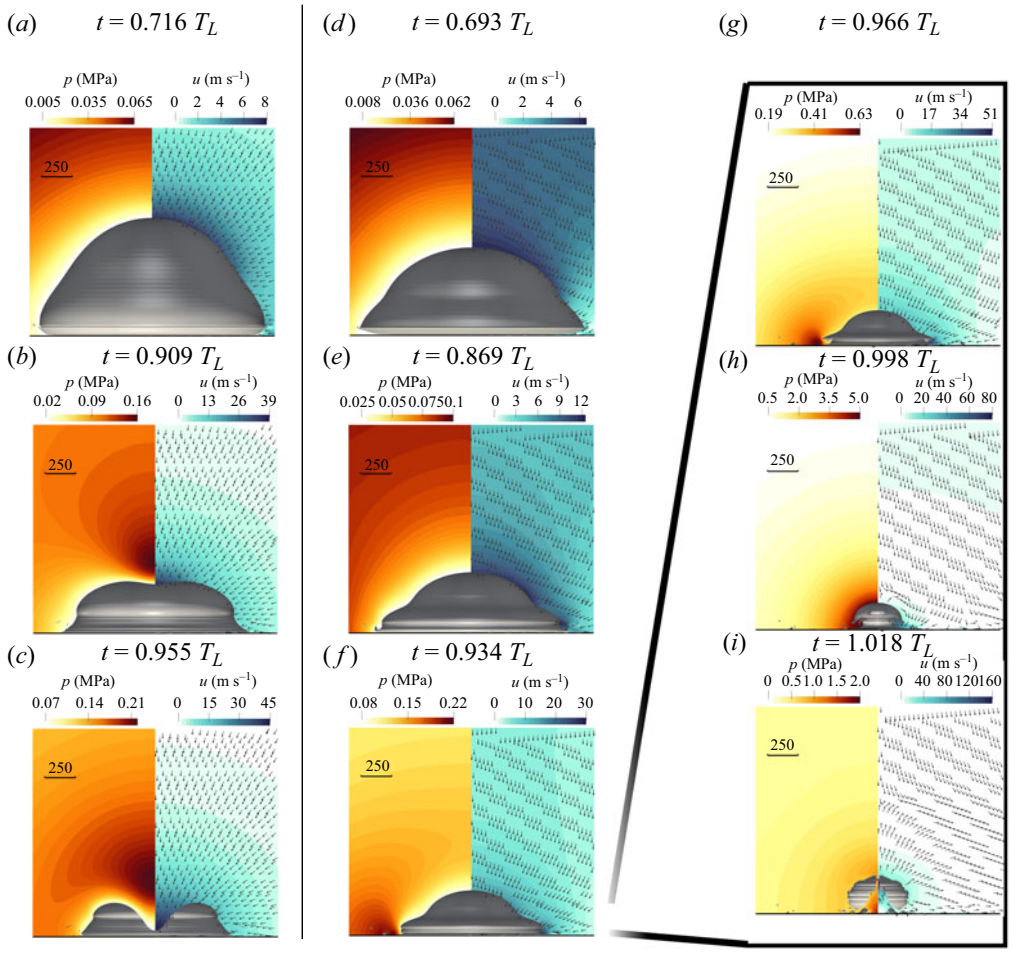

Figure 10. Bubble shape, pressure and velocity field at different time instances during the collapse of the bubble initially located at $d = 290\,\mu\text{m}$ ($\gamma = 0.37$ and 0.43, respectively). (*a–c*) In quiescent water ($v_{jet} = 0\,\text{m}\,\text{s}^{-1}$). The lifetime of this bubble is $T_L = 181.6\,\mu\text{s}$. (*d–i*) Subject to a wall jet with $v_{jet} = 5\,\text{m}\,\text{s}^{-1}$. The lifetime of this bubble is $T_L = 155.3\,\mu\text{s}$. The scale bar corresponds to $250\,\mu\text{m}$.

In figure 13 the jetting behaviour as a function of stand-off and wall jet velocity is presented. In this parameter map we divide the jetting behaviour into four regimes. First, the regular jet, i.e. the rather broad/thick/wide jet that is directed axially towards the wall, being a few hundred micrometres in diameter and reaching typical velocities of 50–150 $\text{m}\,\text{s}^{-1}$ (green). Second, the splitting regime, in which the rather symmetric bubble splits upon the convergence of the planar jet (red) with the generation of two oppositely directed jets. Third, the needle-jet regime, i.e. the convergence of the planar jet that results in a much faster jet axially directed toward the wall (blue). And fourth, the detachment regime, where the planar convergent jet runs at the wall pushing between the bubble and wall, converging before the regular jet pierces the bubble, resulting in bubble lift-off (magenta).

Figure 13 shows how certain regimes extend to larger stand-off values with increasing wall jet velocity. For example, the needle-jet regime, in a quiescent liquid only occurring for $\gamma \lessapprox 0.2$, extends to larger stand-offs of about $\gamma \approx 0.8$ for $v_{jet} = 5\,\text{m}\,\text{s}^{-1}$. Similarly,

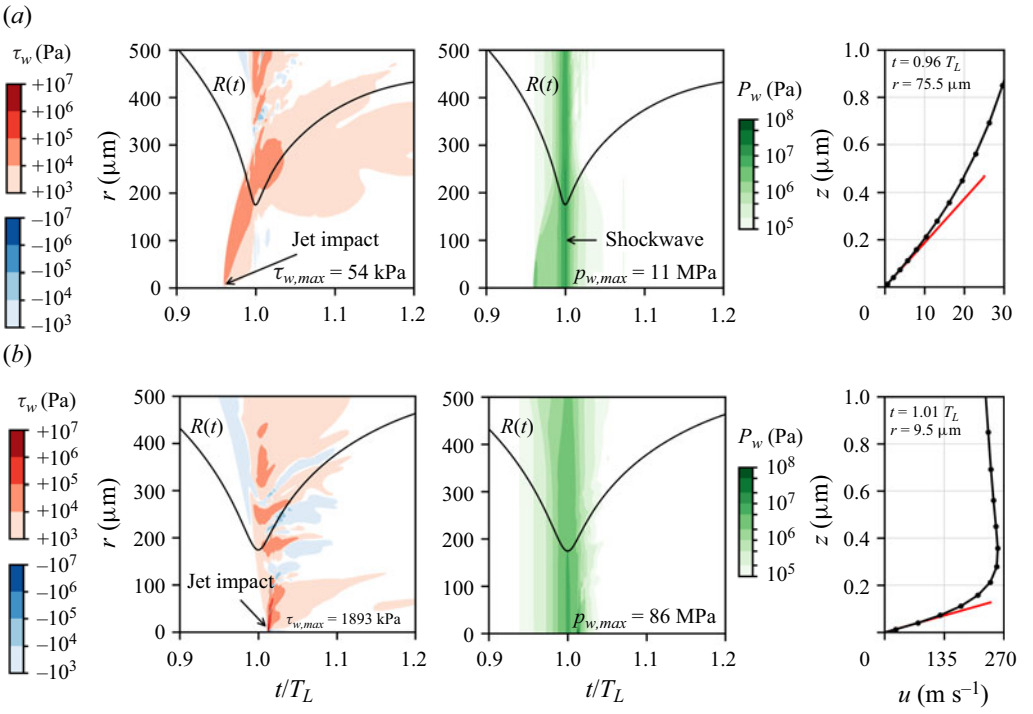

Figure 11. Space–time plots of the wall shear stress τ_w and the wall pressure p_w, and profile of the radial velocity u of the liquid at the location of the highest wall shear rate, of the bubble initially located at $d = 290\,\mu$m. In the space–time plots, the black line shows the volume-equivalent bubble radius $R(t)$ and, with respect to τ_w, red (blue) areas indicate a radially outward (inward) going flow. In the plots of the velocity profiles, the red line represents the velocity gradient associated with $\tau_{w,max}$, and the black dots show the locations of the cell centres of the applied computational mesh. Results are shown for (*a*) $v_{jet} = 0\,\mathrm{m\,s^{-1}}$, $\gamma = 0.37$; (*b*) $v_{jet} = 5\,\mathrm{m\,s^{-1}}$, $\gamma = 0.43$.

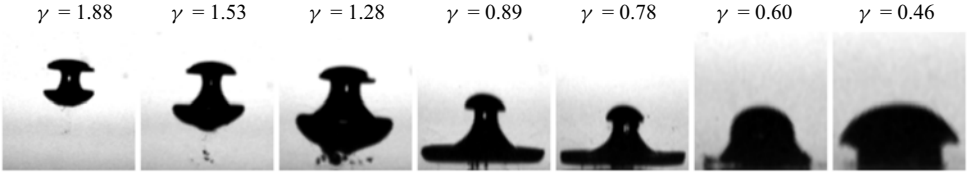

Figure 12. Bubble shape in the last instance before the collapse for different stand-off distances γ (indicated above each frame) with the constant wall jet velocity of $v_{jet} = 5\,\mathrm{m\,s^{-1}}$. The wall coincides with the bottom in all frames. The scale differs in the frames.

the detachment regime is reported in quiescent conditions for $\gamma \approx 0.2$, but not $\gamma = 0.1$ (Abedini, Hanke & Reuter 2023), and occurs here up to $\gamma \approx 0.6$.

Under some conditions both the regular jet and a needle jet or splitting is observed; see, for example, the $v_{jet} = 1.6\,\mathrm{m\,s^{-1}}$ row, indicated by the stacked symbols. The corresponding dynamics is shown in Appendix B in more detail.

4. Summary and discussion

Under the assumption of two-dimensional axisymmetry, the maximum wall shear stress and wall pressure recorded in the conducted simulations may be considered as lower bounds of these quantities, since full mesh convergence of these quantities could not

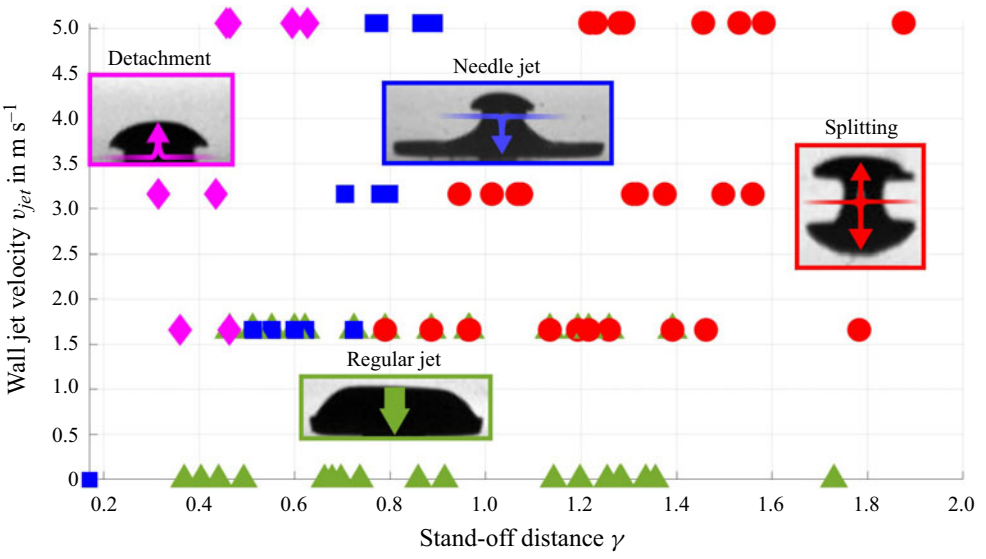

Figure 13. Parameter overview. Splitting regime (red dots), needle-jet regime (blue squares), detachment regime (magenta diamonds) and regular jetting regime (green triangles) are shown. The arrows on the example pictures indicate the main jetting direction during the collapse. With needle-jet data for $v_{jet} = 0\,\mathrm{m\,s^{-1}}$ from Reuter & Ohl (2021).

be achieved with the available computing resources. Taking the case of the bubble initially located at $d = 290\,\mu\mathrm{m}$ and subject to wall jet with a velocity of $v_{jet} = 5\,\mathrm{m\,s^{-1}}$ as an example, the space–time plots of the wall shear stress and wall pressure obtained on meshes with $\Delta x_0 \in \{1, 2\}\,\mu\mathrm{m}$, shown in figure 14, exhibit very little qualitative differences. The corresponding maximum values for the wall shear stress and wall pressure obtained on meshes with $\Delta x_0 \in \{1, 2, 4\}\,\mu\mathrm{m}$ are shown in figure 15. A converging trend towards higher peak values can be observed as the mesh is refined. Furthermore, the time at which the peak values occur exhibits a negligible difference between the results obtained on meshes with $\Delta x_0 = 1$ and $\Delta x_0 = 2\,\mu\mathrm{m}$. This is consistent with previous studies regarding the cavitation-generated wall pressure (Mihatsch, Schmidt & Adams 2015; Trummler, Schmidt & Adams 2021), which demonstrated that the maximum wall pressure is strongly mesh dependent, with increasing peak values for decreasing mesh spacing. Note that the centres of the mesh cells closest to the wall are located at a distance of only 12.5 nm ($\Delta x_0 = 1\,\mu\mathrm{m}$) and 25 nm ($\Delta x_0 = 2\,\mu\mathrm{m}$), highlighting the extreme resolution requirements of these simulations. However, the maximum jet velocity generated in experimental settings is limited by the symmetry of the needle-jet generation (Gordillo & Blanco-Rodríguez 2023) and the jet stability (Reuter *et al.* 2022*a*). Both effects cannot be covered in axisymmetric simulations.

In cavitation-solid interactions, jetting is a key aspect as it shapes the bubble dynamics and is directly interacting with the wall. The pressure gradient of a stagnation point flow alters the jetting behaviour and the bubble dynamics significantly. The bubble translates with the flow towards the wall while the pressure gradient caused by the stagnation flow tends to push the bubble away from the wall (Blake *et al.* 2015). As a consequence of the opposing pressure gradients, the bubble takes an oblate shape that is decisive for the further bubble dynamics. During collapse, the oblate bubble develops a planar converging jet. This planar jet shapes the initially oblate bubble to an hourglass shape and can even result in bubble pinch-off. These dynamics were studied by Starrett (1982) and in

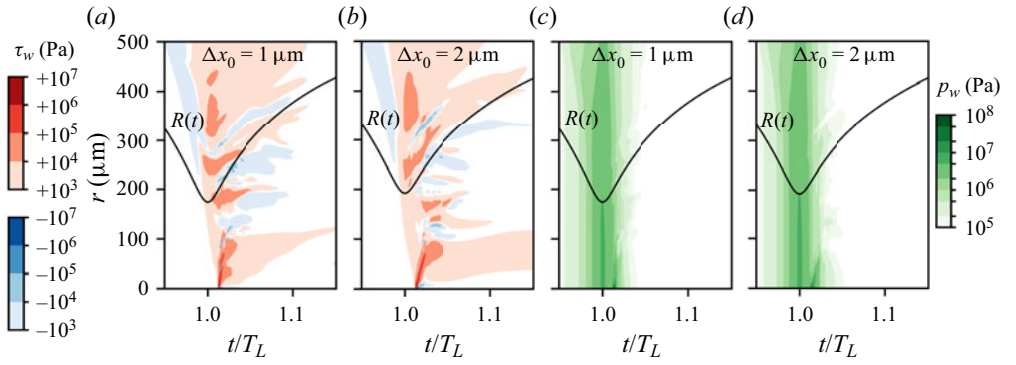

Figure 14. Space–time plots of the wall shear stress τ_w and the wall pressure p_w of the bubble initially located at $d = 290\,\mu\text{m}$ and subject to wall jet with a velocity of $v_{jet} = 5\,\text{m}\,\text{s}^{-1}$, obtained on computational meshes with a mesh spacing of $\Delta x_0 = 1\,\mu\text{m}$ and $\Delta x_0 = 2\,\mu\text{m}$. In the space–time plots, the black line shows the volume-equivalent bubble radius $R(t)$ and, with respect to τ_w, red (blue) areas indicate a radially outward (inward) going flow.

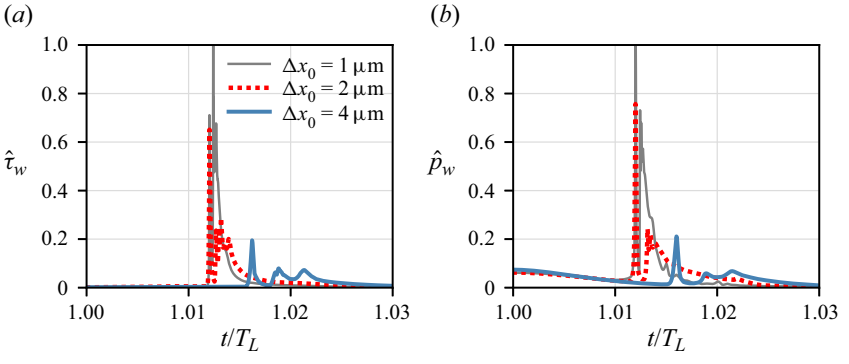

Figure 15. Maximum wall shear stress $\hat{\tau}_w$ and maximum wall pressure $\hat{p}_w$, normalized by the respective values on the finest mesh ($\Delta x_0 = 1\,\mu\text{m}$), of the bubble initially located at $d = 290\,\mu\text{m}$ and subject to wall jet with a velocity of $v_{jet} = 5\,\text{m}\,\text{s}^{-1}$, as a function of time obtained on computational meshes with a mesh spacing of $\Delta x_0 \in \{1, 2, 4\}\,\mu\text{m}$.

numerical studies by Blake and co-workers (Blake *et al.* 1986; Robinson & Blake 1994; Blake *et al.* 2015) for rather large bubble-to-wall stand-offs and is a general feature of the collapse of an oblate-spheroidally shaped bubble even without stagnation flow (Chapman & Plesset 1972; Voinov & Voinov 1975; Shima & Sato 1979).

When the planar jet converges onto the slender gas volume on the axis of symmetry, a high-pressure stagnation point occurs, the gas phase collapses and a thin needle jet is ejected along the axis of symmetry (Gordillo & Blanco-Rodríguez 2023). This type of jetting has also been shown to occur in stagnant liquid, but only for the smallest bubble-to-wall stand-offs of about $\gamma \lessapprox 0.2$ (Lechner *et al.* 2019; Reuter & Ohl 2021; Bußmann *et al.* 2023). This regime is extended to larger stand-offs with the stagnation flow.

The needle jet at larger stand-offs stimulated by the stagnation flow allows achieving about 40 times higher wall shear at only around 5 times larger wall pressures. The simulations show that at the wall the jet impact pressures in the stagnation flow case are larger than the bubble collapse pressures, which stands in contrast to the bubble dynamics

in stagnant flow, where only regular jetting occurs, and the collapse pressures are larger than jet impact pressures.

Recently, it has been shown that only the bubble collapse directly at the wall is erosive, which occurs for $\gamma \lessapprox 0.2$ for a stagnant liquid (Reuter *et al.* 2022*a*). It is fascinating to observe that the bubble in the small γ regime does not collapse at the wall, but lifts off and collapses $\approx$120 µm away in the bulk, and indeed, we did not find indications of material damage on our glass samples here. Consistently, the maximum wall shear stresses, and wall pressures found here over the entire range of stand-off distances stay mainly below the yield strength and tensile strength of most metals or metal alloys, such as silver with 55 MPa and 110–340 MPa, respectively, (Smith & Fickett 1995) and stainless steel 316 L with 440 and 1020 MPa, respectively (Franc 2009).

The adjustment of the wall jet flow velocity and the stand-off distance allows us to control the behaviour of the bubble precisely and, thus, achieve a tailored interaction with the wall. Due to the rich bubble dynamics, a wide range of applications is possible. One example is a cavitation bubble at a small stand-off distance to the wall in a wall jet flow with sufficient velocity. Here, high wall shear stress can be achieved when the jet hits the wall, which can be used for precision cleaning. At the same time, the bubble detaches from the wall and, thus, is not in contact with the wall during the collapse. We anticipate that this could avoid material damage.

5. Conclusion

We studied the dynamics of a single cavitation bubble close to a wall in the stagnation flow of a wall jet. Using high-speed imaging together with numerical simulations, which provide quantitative insight into the produced wall shear stresses and wall pressures, we found that a wall jet flow of already rather small velocities, i.e. of less than 10 m s, can shape the bubble and significantly change its dynamics. As a result, wall shear stresses and pressures exerted onto the nearby wall are altered drastically. For example, the wall shear stresses, which are crucial in surface cleaning, can be increased by a factor of 44 as compared with the stagnant case and reach values above 2700 kPa here. At the same time, the wall pressures, which are considered a prime cause for cavitation erosion, are increased by only a factor of six as compared with the stagnant case and reach values of 49 MPa, i.e. stay below typical material damage thresholds.

As cavitation bubbles in a stagnant liquid have been shown to be erosive only when they collapse directly at the wall, it is an important finding that a cavitation bubble in the wall jet, somewhat counterintuitively, can lift off the wall just before its collapse and migrate against the wall jet flow direction such that its collapse occurs without wall contact.

The mechanisms of how the wall jet alters the bubble dynamics can be understood via the oblate, ellipsoidal shaping of the bubble by the wall jet. This stimulates the formation of wall-parallel and convergent planar jets. They are also the origin of needle-jet formation and, consequently, the needle-jet regime, in stagnant liquid only found for bubbles at very small stand-offs, extends further into larger stand-off ranges with increasing wall jet velocities.

As the wall jet is technologically rather easy to implement, our results suggest it can be exploited to tailor bubble–wall interactions in terms of stresses on the wall and their distribution, with potential applications, for example, in material peening and hardening, surface cleaning and erosion prevention.

Supplementary movies. Supplementary movies are available at https://doi.org/10.1017/jfm.2023.1048.

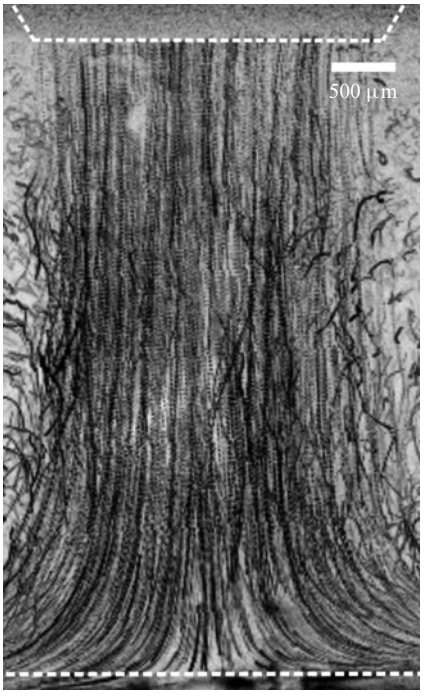

Figure 16. Side view showing the pathlines obtained from microscopic particles seeded into the wall jet flow and recorded with a high-speed camera. The top lines indicate the nozzle exit and the bottom line the position of the wall, $v_{jet} = 5\,\mathrm{m\,s^{-1}}$.

Funding. We thank the Alfred Kärcher Foundation and the DFG through INST 272/280-1 for their financial support.

Declaration of interests. The authors report no conflict of interest.

Author ORCIDs.
Dominik Mnich https://orcid.org/0009-0001-5303-893X;
Fabian Reuter https://orcid.org/0000-0002-8908-4209;
Fabian Denner https://orcid.org/0000-0001-5812-061X;
Claus-Dieter Ohl https://orcid.org/0000-0001-5333-4723.

Appendix A. Flow field

To observe the flow profile of the wall jet, we add particles with about 20 µm in diameter to the liquid and record their motion with a high-speed camera. Eighty images recorded with a frame rate of 200 000 are summed up to obtain pathlines of the nozzle flow, as shown in figure 16 for a flow velocity of $v_{jet} = 5\,\mathrm{m\,s^{-1}}$. At the top, the flow leaves the nozzle exit and it impinges onto the wall at the bottom of figure 16. Then the flow spreads radially outwards, yet it remains mostly laminar without much of a recirculation or disturbance.

Appendix B. Transition regimes

An example of a bubble that shows pinch-off from the planar jet flow and that gets also pierced by the regular jet is presented in figure 17 for a bubble at $\gamma = 0.96$. Between $t = 0.919$ and 0.939, the planar flow meets at the axis of symmetry and results in the

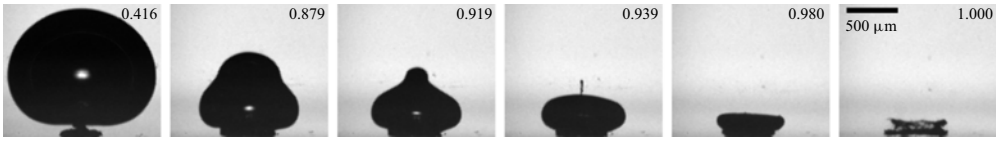

Figure 17. Bubble shape at $\gamma = 0.96$ and $v_{jet} = 1.6\,\mathrm{m\,s^{-1}}$ with both the regular jet and planar jet resulting in pinch-off. The normalized time is indicated in each frame, the bubble lifetime is $T_L = 149\,\mu\mathrm{s}$. A movie of this series is provided as movie 4 in the supplementary material.

collapsed string-like gas phase along the axis of symmetry. However, probably due to the limited momentum associated with the planar flow, at later times the regular jet pierces the bubble and results in the torus collapse geometry known from quiescent liquid.

References

Abedini, M., Hanke, S. & Reuter, F. 2023 In situ measurement of cavitation damage from single bubble collapse using high-speed chronoamperometry. *Ultrason. Sonochem.* **92**, 106272.

Aganin, A.A., Kosolapova, L.A. & Malakhov, V.G. 2019 Dynamics of a spheroidal gas bubble near a rigid surface. *J. Phys.: Conf. Ser.* **1328**, 012043.

Ando, K., Sakota, R., Usui, H., Ishibashi, T., Matsuo, H. & Watanabe, K. 2023 Optimal injection distance in ultrasonic water flow cleaning. *Solid State Phenom.* **346**, 258–262.

Ando, K., Sugawara, M., Sakota, R., Ishibashi, T., Matsuo, H. & Watanabe, K. 2021 Particle removal in ultrasonic water flow cleaning: role of cavitation bubbles as cleaning agents. *Solid State Phenom.* **314**, 218–221.

Benjamin, T.B. & Ellis, A.T. 1966 The collapse of cavitation bubbles and the pressures thereby produced against solid boundaries. *Phil. Trans. R. Soc. Lond.* A **260** (1110), 221–240.

Blake, J.R. & Gibson, D.C. 1987 Cavitation bubbles near boundaries. *Annu. Rev. Fluid Mech.* **19**, 99–123.

Blake, J.R., Leppinen, D.M. & Wang, Q. 2015 Cavitation and bubble dynamics: the Kelvin impulse and its applications. *Interface Focus* **5** (5), 1–15.

Blake, J.R., Taib, B.B. & Doherty, G. 1986 Transient cavities near boundaries. Part 1. Rigid boundary. *J. Fluid Mech.* **170**, 479–497.

Brujan, E.A., Nahen, K., Schmidt, P. & Vogel, A. 2001 Dynamics of laser-induced cavitation bubbles near an elastic boundary. *J. Fluid Mech.* **433**, 251–281.

Bussmann, A., Riahi, F., Gökce, B., Adami, S., Barcikowski, S. & Adams, N.A. 2023 Investigation of cavitation bubble dynamics near a solid wall by high-resolution numerical simulation. *Phys. Fluids* **35** (1), 016115.

Chahine, G.L. 1982 Experimental and asymptotic study of nonspherical bubble collapse. In *Mechanics and Physics of Bubbles in Liquids* (ed. L. van Wijngaarden), pp. 187–197. Springer.

Chapman, R.B. & Plesset, M.S. 1972 Nonlinear effects in the collapse of a nearly spherical cavity in a liquid. *Trans. ASME J. Fluids Engng* **94** (1), 142–145.

Denner, F., Evrard, F. & van Wachem, B. 2020*a* Conservative finite-volume framework and pressure-based algorithm for flows of incompressible. Ideal-gas and real-gas fluids at all speeds. *J. Comput. Phys.* **409**, 109348.

Denner, F., Evrard, F. & van Wachem, B. 2020*b* Modeling acoustic cavitation using a pressure-based algorithm for polytropic fluids. *Fluids* **5** (2), 69.

Denner, F. & Schenke, S. 2023 Modeling acoustic emissions and shock formation of cavitation bubbles. *Phys. Fluids* **35** (1), 012114.

Denner, F., Xiao, C.-N. & van Wachem, B. 2018 Pressure-based algorithm for compressible interfacial flows with acoustically-conservative interface discretisation. *J. Comput. Phys.* **367**, 192–234.

Dijkink, R. & Ohl, C.-D. 2008 Measurement of cavitation induced wall shear stress. *Appl. Phys. Lett.* **93** (25), 254107.

Franc, J.P. 2009 Incubation time and cavitation erosion rate of work-hardening materials. *Trans. ASME J. Fluids Engng* **131** (2), 0213031–02130314.

Gac, S.L., Zwaan, E., Berg, A.V.D. & Ohl, C.-D. 2007 Sonoporation of suspension cells with a single cavitation bubble in a microfluidic confinement. *Lab on a Chip* **7** (12), 1666–1672.

Gibson, D.C. & Blake, J.R. 1982 The growth and collapse of bubbles near deformable surfaces. *Appl. Sci. Res.* **38**, 215–224.

GLAUERT, M.B. 1956 The wall jet. *J. Fluid Mech.* **1** (6), 625–643.
GONZALEZ-AVILA, S.R., DENNER, F. & OHL, C.-D. 2021 The acoustic pressure generated by the cavitation bubble expansion and collapse near a rigid wall. *Phys. Fluids* **33** (3), 032118.
GONZALEZ-AVILA, S.R., HUANG, X., QUINTO-SU, P.A., WU, T. & OHL, C.D. 2011*a* Motion of micrometer sized spherical particles exposed to a transient radial flow: attraction, repulsion, and rotation. *Phys. Rev. Lett.* **107** (7), 1–4.
GONZALEZ-AVILA, S.R., KLASEBOER, E., KHOO, B.C. & OHL, C.D. 2011*b* Cavitation bubble dynamics in a liquid gap of variable height. *J. Fluid Mech.* **682**, 241–260.
GORDILLO, J.M. & BLANCO-RODRÍGUEZ, F.J. 2023 Theory of the jets ejected after the inertial collapse of cavities with applications to bubble bursting jets. *Phys. Rev. Fluids* **8**, 073606.
KIM, W., KIM, T.H., CHOI, J. & KIM, H.Y. 2009 Mechanism of particle removal by megasonic waves. *Appl. Phys. Lett.* **94** (8), 1–4.
KNAPP, R.T. 1955 Recent investigations of the mechanics of cavitation and cavitation damage. *Trans. Am. Soc. Mech. Engrs* **77** (7), 1045–1054.
KOCH, M., LECHNER, C., REUTER, F., KÖHLER, K., METTIN, R. & LAUTERBORN, W. 2016 Numerical modeling of laser generated cavitation bubbles with the finite volume and volume of fluid method using OpenFOAM. *Comput. Fluids* **126**, 71–90.
KOUKOUVINIS, P., STROTOS, G., ZENG, Q., GONZALEZ-AVILA, S.R., THEODORAKAKOS, A., GAVAISES, M. & OHL, C.-D. 2018 Parametric investigations of the induced shear stress by a laser-generated bubble. *Langmuir* **34** (22), 6428–6442.
LAUER, E., HU, X.Y., HICKEL, S. & ADAMS, N.A. 2012 Numerical modelling and investigation of symmetric and asymmetric cavitation bubble dynamics. *Comput. Fluids* **69**, 1–19.
LAUTERBORN, W. & BOLLE, H. 1975 Experimental investigations of cavitation-bubble collapse in the neighbourhood of a solid boundary. *J. Fluid Mech.* **72** (2), 391–399.
LAUTERBORN, W. & KURZ, T. 2010 Physics of bubble oscillations. *Rep. Prog. Phys.* **73** (10), 106501.
LE MÉTAYER, O. & SAUREL, R. 2016 The noble-abel stiffened-gas equation of state. *Phys. Fluids* **28** (4), 046102.
LECHNER, C., LAUTERBORN, W., KOCH, M. & METTIN, R. 2019 Fast, thin jets from bubbles expanding and collapsing in extreme vicinity to a solid boundary: a numerical study. *Phys. Rev. Fluids* **4** (2), 1–7.
LECHNER, C., LAUTERBORN, W., KOCH, M. & METTIN, R. 2020 Jet formation from bubbles near a solid boundary in a compressible liquid: numerical study of distance dependence. *Phys. Rev. Fluids* **5** (9), 093604.
LIANG, X.-X., LINZ, N., FREIDANK, S., PALTAUF, G. & VOGEL, A. 2022 Comprehensive analysis of spherical bubble oscillations and shock wave emission in laser-induced cavitation. *J. Fluid Mech.* **940**, A5.
MIFSUD, J., LOCKERBY, D.A., CHUNG, Y.M. & JONES, G. 2021 Numerical simulation of a confined cavitating gas bubble driven by ultrasound. *Phys. Fluids* **33** (12), 122114.
MIHATSCH, M.S., SCHMIDT, S.J. & ADAMS, N.A. 2015 Cavitation erosion prediction based on analysis of flow dynamics and impact load spectra. *Phys. Fluids* **27** (10), 103302.
OHL, C.D., ARORA, M., DIJKINK, R., JANVE, V. & LOHSE, D. 2006*a* Surface cleaning from laser-induced cavitation bubbles. *Appl. Phys. Lett.* **89** (7), 074102.
OHL, C.D., ARORA, M., IKINK, R., DE JONG, N., VERSLUIS, M., DELIUS, M. & LOHSE, D. 2006*b* Sonoporation from jetting cavitation bubbles. *Biophys. J.* **91** (11), 4285–4295.
PHILIPP, A. & LAUTERBORN, W. 1998 Cavitation erosion by single laser-produced bubbles. *J. Fluid Mech.* **361**, 75–116.
PLESSET, M.S. & CHAPMAN, R.B. 1971 Collapse of an initially spherical vapour cavity in the neighbourhood of a solid boundary. *J. Fluid Mech.* **47** (2), 283–290.
PRENTICE, P., CUSCHIERI, A., DHOLAKIA, K., PRAUSNITZ, M. & CAMPBELL, P. 2005 Membrane disruption by optically controlled microbubble cavitation. *Nat. Phys.* **1** (2), 107–110.
REUTER, F., DEITER, C. & OHL, C.-D. 2022*a* Cavitation erosion by shockwave self-focusing of a single bubble. *Ultrason. Sonochem.* **90**, 106131.
REUTER, F. & KAISER, S.A. 2019 High-speed film-thickness measurements between a collapsing cavitation bubble and a solid surface with total internal reflection shadowmetry. *Phys. Fluids* **31** (9), 097108.
REUTER, F., LAUTERBORN, S., METTIN, R. & LAUTERBORN, W. 2017 Membrane cleaning with ultrasonically driven bubbles. *Ultrason. Sonochem.* **37**, 542–560.
REUTER, F. & METTIN, R. 2016 Mechanisms of single bubble cleaning. *Ultrason. Sonochem.* **29**, 550–562.
REUTER, F. & METTIN, R. 2018 Electrochemical wall shear rate microscopy of collapsing bubbles. *Phys. Rev. Fluids* **3** (6), 063601.

REUTER, F. & OHL, C.D. 2021 Supersonic needle-jet generation with single cavitation bubbles. *Appl. Phys. Lett.* **118** (13), 134103.

REUTER, F., ZENG, Q. & OHL, C.-D. 2022*b* The Rayleigh prolongation factor at small bubble to wall stand-off distances. *J. Fluid Mech.* **944**, A11.

ROBINSON, P.B. & BLAKE, J.R. 1994 Dynamics of cavitation bubble interactions. In *Bubble Dynamics and Interface Phenomena* (ed. J.R. Blake, J.M. Boulton-Stone & N.H. Thomas), pp. 55–64. Springer.

SAINI, M., TANNE, E., ARRIGONI, M., ZALESKI, S. & FUSTER, D. 2022 On the dynamics of a collapsing bubble in contact with a rigid wall. *J. Fluid Mech.* **948**, A45.

SHIMA, A. & SATO, Y. 1979 The collapse of a spheroidal bubble near a solid wall. *Ingenieur-Archiv.* **48**, 85–95.

SMITH, D.R. & FICKETT, F.R. 1995 Low-temperature properties of silver. *J. Res. Natl Inst. Stand. Technol.* **100** (2), 119.

STARRETT, J.E. 1982 Bubble dynamics in stagnation flow. PhD thesis, University of California.

SUPPONEN, O., OBRESCHKOW, D., TINGUELY, M., KOBEL, P., DORSAZ, N. & FARHAT, M. 2016 Scaling laws for jets of single cavitation bubbles. *J. Fluid Mech.* **802**, 263–293.

TOMITA, Y. & SHIMA, A. 1986 Mechanisms of impulsive pressure generation and damage pit formation by bubble collapse. *J. Fluid Mech.* **169**, 535–564.

TRUMMLER, T., SCHMIDT, S.J. & ADAMS, N.A. 2021 Effect of stand-off distance and spatial resolution on the pressure impact of near-wall vapor bubble collapses. *Intl J. Multiphase Flow* **141**, 103618.

VOINOV, O.V. & VOINOV, V.V. 1975 Numerical method of calculating nonstationary motions of an ideal incompressible fluid with free surfaces. **221** (3), 559–562.

ZENG, Q., AN, H. & OHL, C.-D. 2022 Wall shear stress from jetting cavitation bubbles: influence of the stand-off distance and liquid viscosity. *J. Fluid Mech.* **932**, A14.

ZENG, Q., GONZALEZ-AVILA, S.R., DIJKINK, R., KOUKOUVINIS, P., GAVAISES, M. & OHL, C.-D. 2018 Wall shear stress from jetting cavitation bubbles. *J. Fluid Mech.* **846**, 341–355.

ZENG, Q., GONZALEZ-AVILA, S.R. & OHL, C.D. 2020 Splitting and jetting of cavitation bubbles in thin gaps. *J. Fluid Mech.* **896**, 1–28.

ZHANG, S., DUNCAN, J.H. & CHAHINE, G.L. 1993 The final stage of the collapse of a cavitation bubble near a rigid wall. *J. Fluid Mech.* **257**, 147–181.